CHALMERS
UNIVERSITY OF TECHNOLOGY

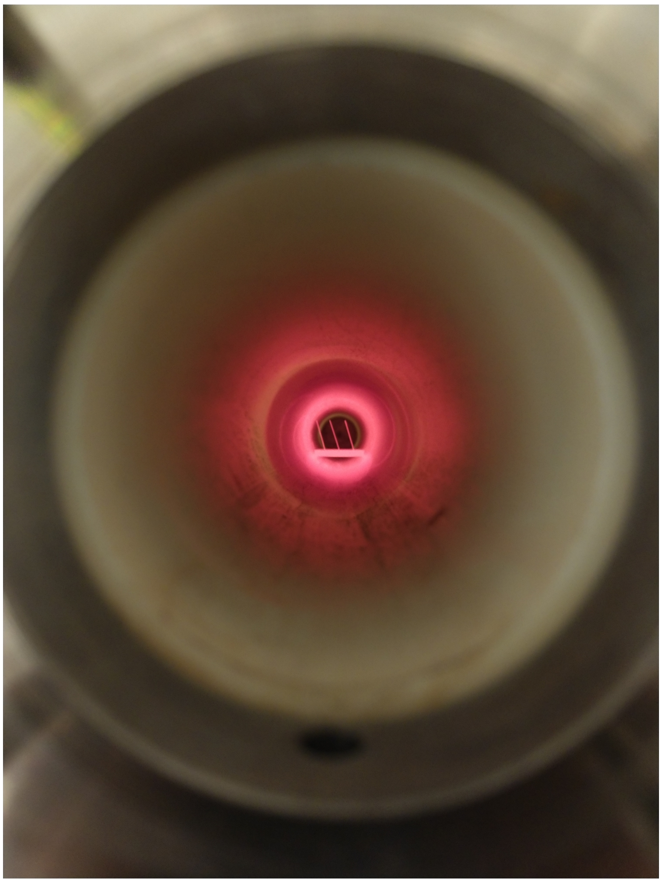

Corrosion behaviour of ferritic stainless steels in H2/H2O environments

Studying the effects of dilution in simulated electrolysis environments

Department of Chemistry and Chemical Engineering

ISAK ALMYREN

DIVISION OF ENERGY AND MATERIALS
CHALMERS UNIVERSITY OF TECHNOLOGY
Gothenburg, Sweden 2023
www.chalmers.se

MASTER'S THESIS 2023

Corrosion behaviour of ferritic stainless steels in H2/H2O environments

Studying the effects of dilution in simulated electrolysis environments

Isak Almyren

Department of Chemistry and Chemical Engineering
Division Energy and Materials
Environmental Inorganic Chemistry
CHALMERS UNIVERSITY OF TECHNOLOGY
Gothenburg, Sweden 2023

Corrosion behaviour of ferritic stainless

steels in H_2/H_2O environments
Studying the effects of dilution in simulated electrolysis environments
ISAK ALMYREN

Supervisor: Dr. Anton Chyrkin, Inorganic Environmental Chemistry
Examiner: Prof. Jan Froitzheim, Inorganic Environmental Chemistry

Master's Thesis 2023
Department of Chemistry and Chemical Engineering
Division of Energy and Materials
Inorganic Environmental Chemistry, SOFC Group
Chalmers University of Technology
SE-412 96 Gothenburg
Telephone +46 31 772 1000

Cover: Metal samples exposed in a high temperature furnace

Typeset in LaTeX
Printed by Chalmers Reproservice
Gothenburg, Sweden 2023

Abstract

Solid Oxide Electrolysis Cells (SOEC) is an emerging technology for green hydrogen production with high efficiency and without a need for precious metal catalysts. SOEC operates at high temperatures which creates some challenges for the system, one being the high temperature corrosion of metal components in the electrolysis cell. During the thesis work, potential steels for use in SOEC have been exposed in simulated fuel side electrolysis environments (H_2/H_2O), with varying degrees of argon gas dilution.

The work found severe corrosion at 650 ℃ , with a large amount of Fe rich oxides forming for both AISI 441 and 22 Crofer APU. Due to samples experiencing breakaway corrosion samples were pre-oxidised for long term exposures. Different pre-oxidation times was performed and it was found that increasing pre-oxidation time increased corrosion protection. During long term exposures, formation of hematite (Fe_2O_3) was identified. Hematite was calculated to be thermodynamically unstable at the specified (H_2/H_2O) environments. A potential cause of the hematite formation was studied; that the Water-Hydrogen-Oxygen reaction did not come to chemical equilibrium and thus causing a shift in p(O_2) in the furnace. Platinum was added to catalyse this reaction before reaching the samples. This addition generally diminished the rate of corrosion but was unable to completely stop the formation of hematite.

Further work is required for better understanding of the dilution effect and its dependence on temperature as well as the causes of hematite formation. Updated experimental setups should be designed as this method causes difficulties not well understood.

Keywords: SOEC, Electrolysis, high temperature corrosion, hydrogen, steam, fuel environments, dilution, hematite

Acknowledgements

First, I would like to thank my supervisor Anton Chyrkin, for the never ending supply of ideas and for always suggesting a way forward. I would also like to thank my examiner Jan Froitzheim for his perpetually open door and great insights on my continued work. I of course also want to thank Reddy, Matthieu, Jan-Erik, and Hlib as they have been very helpful throughout my work, from tips and tricks in the lab to fika and uplifting conversations throughout my time at the department. I would also like to thank Vadna Kumari Gupta for her assistance in Raman spectroscopy.

I would like to extend another huge thank you to my friends and family. My friends Eva, Jelka, Leyla, and Kennet are the reason I have made it through this degree with intense exam weeks cramped up in a study room filled with sandwiches and infinite amounts of fika. And Lovisa for making the effort of keeping my work life balance intact as well as the neat pictures of my metal samples that are found in this report.
I would also like to thank my parents for the support in everything I do. When others would have said “shouldn’t you do something more normal?”, my parents said “when do we get to read it?”.

Lastly, I would like to dedicate my thesis to Anton Lind Vazdekis who should have been here with us graduating this year. You will be forever missed.

Isak Almyren, Gothenburg, August 2023

List of Acronyms

Below is the list of acronyms that have been used throughout this thesis listed in alphabetical order:

BIB	Broad Ion Beam
BSE	Backscattered Electrons
CCS	Carbon Capture System
Chromia	Chromium Oxide, Cr_2O_3
EDX	Energy-Dispersive X-ray spectroscopy
EV	Electric Vehicle
FC	Fuel Cell
FCEV	Fuel Cell Electric Vehicle
ΔG	Gibbs Free Energy
M	Metal
PEM	Proton Exchange Membrane
pO_2	Partial pressure of O_2
SE	Secondary Electrons
SEM	Scanning Electron Microscope
SOC	Solid Oxide Cell
SOEC	Solid Oxide Electrolysis Cell
SOFC	Solid Oxide Fuel Cell
TEC	Thermal Expansion Coefficient
XRD	X-ray diffraction
YSZ	Yttria Stabilised Zirconia

Nomenclature

Below is the nomenclature of chemicals that have been used throughout this thesis listed in alphabetical order:

Chemicals

Argon gas	Ar_2
Carbon dioxide	CO_2
Carbon monoxide	CO
Chromia	Cr_2O_3
Chromium	Cr
Corundum	Crystal structure of Chromia and Hematite
Electron	e^-
Hematite	Fe_2O_3
Hydrogen gas	H_2
Iron	Fe
Magnetite	Fe_3O_4
Manganese	Mn
Nickel	Ni
Nicrotal alloy	NiCr
Oxygen anion	O^{-2}
Oxygen gas	O_2
Spinel	Crystal structure of Magnetite
Water	H_2O
Wüstite	FeO

Contents

List of Figures

List of Tables

1

Introduction

Hydrogen is one of the most important chemicals used today, the entire hydrogen market is valued at 155 billion dollars in 2022.[18] Hydrogen has applications in almost all aspects of society, with uses in fertiliser, fuel and speciality chemical production as well as future uses in energy storage and projects such as Hybrit green steel. As of 2021, the annual hydrogen production is 94 million tonnes globally and is projected to increase rapidly in the coming years.[2] The main use of hydrogen globally is in the chemical industry, mainly for the production of ammonia and methanol. Ammonia is used mainly in the production of synthetic fertilisers, and methanol is used in the production of formaldehyde, substituting crude oil in the production of speciality chemicals and fuel production. These sources are important for the global chemical industry and their use is projected to continue to increase over the coming years. Today, both ammonia and methanol are produced almost exclusively with hydrogen from fossil sources, and to reduce carbon emissions from these two industries, the source of the hydrogen must be changed. [17] [2] [14]

There is a national effort to decarbonise the Swedish steel industry through multiple project. The two main projects are Hybrit and H2 green steel. Steel production is historically heavy on carbon emissions, making up 7,2 % of the total emissions globally.[24]Therefore, it is very relevant to reduce CO_2 emissions from this industry, which is why the decarbonisation projects were started. Through the use of hydrogen, the main carbon emitter, the blast furnace, is replaced by a direct reduction of the iron ore with H_2, reducing CO_2 emissions drastically. The potential emissions are instead shifted towards hydrogen production. Decarbonising the steel industry is therefore very dependent on not just hydrogen but green hydrogen specifically.

One of the potential applications for hydrogen technology is to create Fuel cell vehicles to phase out conventional internal combustion engine vehicles. Multiple sectors, such as personal vehicles and mid to long-range transport, have been considered for fuel cell vehicles. In this development race, Fuel Cell Electrical Vehicles (FCEVs) are pitted against Electrical Vehicles (EVs). As of 2020, the FCEV sector is still small with 34 000 registered vehicles compared to 10,2 million EVs currently on roads around the world.[1] Hydrogen is a resource that is often pitched to be used in hard-to-abate sectors, generally industries which is difficult to electrify. Except for the above mentioned chemical and steel industries, long distance freight transportation is another sector with potential application. The main cell type pitched is low temperature cells such as PEM cells, which will not require the high temperatures of SOFCs and can better handle the electrical cycling of an engine. Regardless of type, the development of FCEVs requires production of green hydrogen to be a viable alternative in transportation sectors that are difficult to electrify.

Currently, 95% of the hydrogen produced is the so-called *grey hydrogen*, which comes from fossil sources. Without changing the source of the hydrogen produced, green steel projects, FC vehicles, and chemical production cannot be considered environmentally sustainable. The main source of grey hydrogen is natural gas through steam reforming, turning CH4 into H_2 and CO_2. Methane is reacted with steam, producing hydrogen gas and carbon monoxide, which is then further reacted with more steam to produce more H_2 and turn CO into CO_2. If the process is run with an efficiency conversion of 100%, each mole of H_2 produces 0,25 moles of CO_2. [19] Carbon emissions from steam reformation for each ton of H_2 are between 7,5-12 tones of CO_2.[5] During 2021 120 Mt of H_2 was produced, 47% of which from from natural gas (27% and 22% from coal and oil, respectively). The total emissions for steam reforming are between 423-623 Mt of CO_2 each year, with the other sources such as coal and oil have even higher emissions per ton of H_2 produced. [12]
To reach the climate goals set by the Paris agreement, grey hydrogen has to be replaced by more sustainable ways of production. Two proposed sustainable hydrogen production types are blue and green hydrogen. Blue hydrogen is produced by steam reforming, like grey hydrogen described above, but adds a carbon capture system (CCS) to eliminate the produced CO_2. The promising aspect of CCS is that it can be used to amend already existing production instead of building new hydrogen plants. The other option, green hydrogen, is hydrogen produced in a completely renewable way. The main technology proposed to produce green hydrogen is electrolysis using electricity from renewable sources such as solar or wind power. Assuming that the electricity used is produced completely environmentally friendly by sources such as solar, wind or nuclear, the hydrogen produced can be classified as having a net zero increase in CO_2 emissions. Other proposed technologies exist, but electrolysis is the most promising way of producing green hydrogen. To be able to replace the grey hydrogen used today and to expand the hydrogen market as demand for green hydrogen increases, the annual production will have to reach 306 million tons by the year 2050. [31]

1.1 Aim

Due to the large demand for green hydrogen in the coming years, it is very relevant to study electrolysis technology and its challenges. For electrolysis at high temperatures, stainless steels are used to a high extent in interconnects (further described in section 1.2). Steels face a multitude of problems which are not fully understood. This work aims to further investigate the effects reported by Alnegren et al. relating to a change in corrosion behaviour with changing humidity.
Alnegren found that the increase in total pressure of H_2 and H_2O, while keeping the H_2/H_2O ratio constant, resulted in a higher oxidation rate of nonprotective oxides rich in iron for one of the steels investigated. The observed dilution effect was observed mainly during the first 24 hours of exposure and caused the material AISI

441 to experience different corrosion behaviour, depending on how diluted the gas mix was. It was concluded that the effect was not seen for all materials but that: "[...] the absolute pressure of H_2/H_2O is an important parameter for the selective oxidation of Cr in FeCr alloys". [3]

To further study the effect, this work aims to conduct experiments at lower temperatures. Following the hypothesis that the dilution effect was most prominent during the ramping up of temperature in the work of Alnegren.

1.1.1 Relevant Questions to answer

- How is the corrosion behaviour affected by lowering the temperature from 850 °C to 650 °C?
- What is the extent of the dilution effect at 650°C?
- Are there other effects stemming from Ar-dilution of the gas flow?

1.2 Theoretical Background

1.2.1 Electrolysis

Electrolysis is the electrochemical splitting of water into hydrogen and oxygen. Electricity is applied to an electrochemical cell creating an electrical potential between the cathode and the anode. The general structure of an oxygen anion-conducting electrolysis cell is described in Figure 1.1.

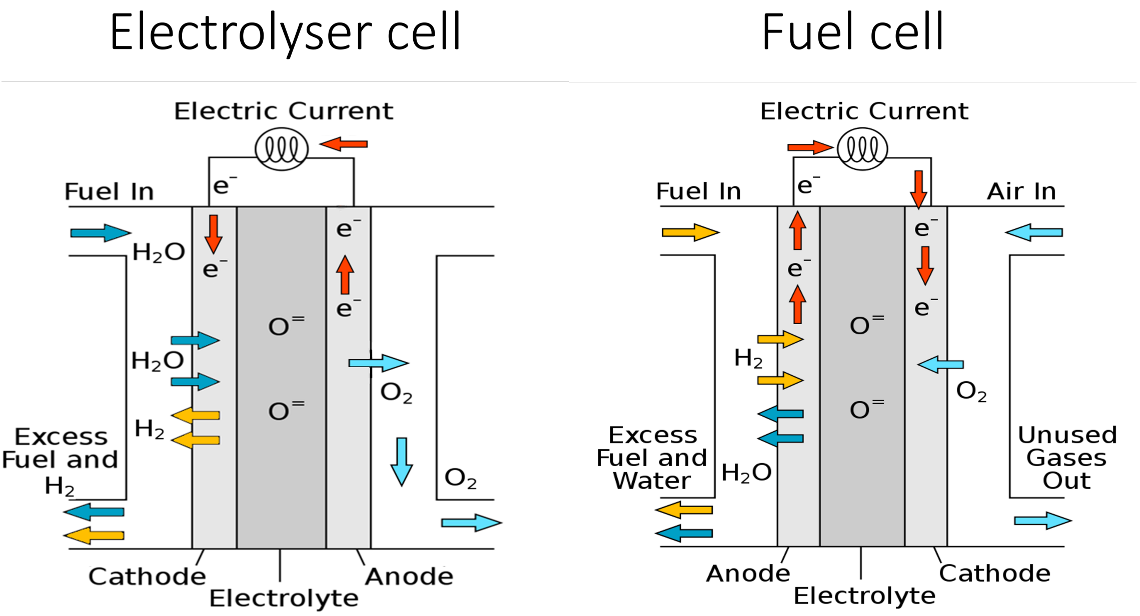
Electrolyser cell

Fuel cell

Figure 1.1: Schematic of an oxygen anion conducting electrolyser cell and fuel cell: containing the anode, electrolyte, cathode, and the connecting circuit.

The chemical reactions that are taking place in the electrolysis cell are described in equations 1.1 and 1.2 with the overall reaction described by equation 1.3

$$\mathit{Reduction} : \mathrm{H_2O} + 2\,\mathrm{e^-} \longrightarrow \mathrm{H_2} + \mathrm{O^{2-}} \tag{1.1}$$

$$\mathit{Oxidation} : \mathrm{O^{2-}} \longrightarrow \frac{1}{2}\,\mathrm{O_2} + 2\,\mathrm{e^-} \tag{1.2}$$

$$\mathit{Overall\ reaction} : \mathrm{H_2O} \longrightarrow \mathrm{H_2} + \frac{1}{2}\,\mathrm{O_2} \tag{1.3}$$

The thermodynamics of the reaction can be described by the free Gibbs energy at standard conditions (25 ℃, 1 atm, 1 mole of H_2), ΔG_0. ΔG_0 indicates if a reaction is spontaneous or not i.e. if the reaction takes place without the need for added energy. The above mentioned reactions take place in an electrochemical cell, ΔG_0 needs to be formulated to fit the system by using the cell potential, E_0, to describe its energy,

$$\Delta G = -nFE \tag{1.4}$$

where G is Gibbs free energy, n is the number of electrons, F is Faraday's constant and E is the cell potential between the anode and cathode. The total cell potential at standard conditions is the sum of the potential between the anode and the cathode,

$$E^0_{cell} = E^0_{ox} + E^0_{red} \tag{1.5}$$

The nerst equation can be used to describe systems which are not operated at ideal conditions,

$$E_{cell} = E^0_{cell} - \frac{RT}{nF} * \ln Q \tag{1.6}$$

Using the cell potential E^0_{cell} for a system under standard conditions and adding $\frac{RT}{nF} * \ln Q$ to describe the actual system at hand with T as temperature and Q as the equilibrium constant for the system. Q is described as the chemical potential of products divided by the chemical potential of reactants,

$$Q = \frac{a_{Products}}{a_{Reactants}} \tag{1.7}$$

and for the general cell reaction 1.3,

$$Q = \frac{[H_2] \cdot [O_2]^{\frac{1}{2}}}{[H_2O]} \tag{1.8}$$

where the activity of the products H_2 and O_2 is divided by the reactant H_2O.

1.2.2 Types of cells

Due to the immense energy required to meet the steep production goal mentioned previously, it is central that the electrolysis process be energy efficient. There are multiple different technologies available for electrolysis such as proton exchange membrane (PEM cells), alkaline, or SOEC. Alkaline electrolysis was the first technology to be developed and is presently the most mature technology, while PEM and SOEC are more in the developmental stage. The potential for SOEC is that the efficiency is projected to be higher than that of other electrolyser technologies, which is why it is interesting to research and develop SOEC technology. [16] [21]

SOEC is operated at relatively high temperatures (600-900 °C) compared to PEM and alkaline, a factor that creates opportunities as well as problems. Electrolysis at high temperatures poses many advantages compared to running it at room temperature. Running the reaction at a higher temperature increases the efficiency of the system by more than 90% when accounting for the combination of electrical and thermal efficiency.[4] Increased temperature also eliminates the need for platinum catalysts and the water management required in low-temperature cells. Solid oxide electrolysis cells consist of an air electrode constructed of a ceramic-metal composite, the most used material is Ni-doped Yttria (Y_2O_3) stabilised zirconia (ZrO_2) (YSZ), an electrolyte made of YSZ and an air electrode where strontium-doped Lanthanum magnetite is the most used material.

The components of SOECs must be able to perform their part of the reaction efficiently; the anode and cathode must facilitate their respective half-cell reactions and the electrolyte should have a high conductivity of O^{2-} ions while maintaining a low electron conductivity. All cell components must have matching Thermal Expansion Coefficients (TEC) to withstand heating and cooling without cracking from mechanical stresses. Cells are placed on top of each other with interconnecting plates in between to form a stack. Interconnecting plates have a double function, they transfer electrons between cells and lead the gas streams to and from both sides of the cell. Historically, the materials used for these interconnects have been ceramics, but due to their poor mechanical qualities and relatively high cost, they have been replaced with stainless steel interconnects.

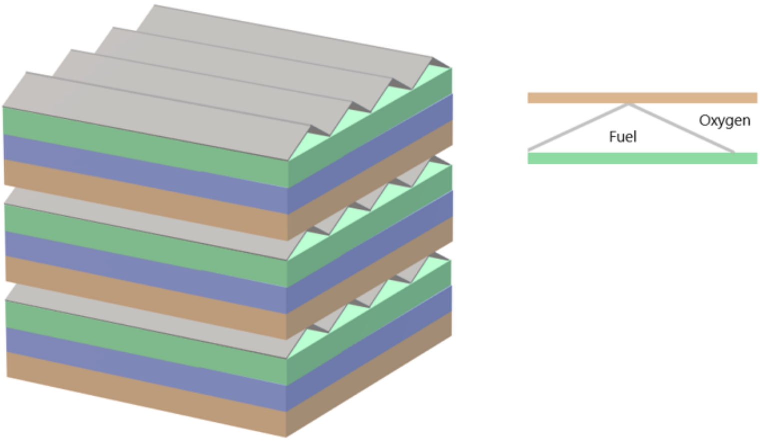

Figure 1.2: A 3D-model of 3 cells forming a SOEC stack. The corrugated interconnect material is represented by the grey layers. The interconnects transfer the fuel gas into the cell and the oxygen out of the cell.

Steel has multiple advantages in that it has good mechanical properties, matching thermal expansion coefficient, low costs, and high electrical conduction, making them a good potential candidate for use in interconnects. Using steel in interconnects also creates new problems, where the most important is the higher rate of degradation compared to ceramics.[29]

This degradation depends mainly on the oxidation of the metal in the electrolyser environments, steam with hydrogen on the fuel side, and pure oxygen (with potential purge gas) on the oxygen side. In commercial stacks, pure steam is used, but when studying the corrosion behaviour in a laboratory setting it is common practise is to dilute the gas with argon, keeping the H_2/H_2O ratio intact while decreasing their total partial pressures. If H_2/H_2O is kept constant, the different environments should be thermodynamically identical and the corrosion behaviour should remain the same.

1.2.3 Ferritic stainless steels

Materials used in SOC tend to be ferritic stainless steels as they correspond well to the requirements of SOC operation. The TEC is a central concept when building SOC stacks. TEC is a factor that describes how materials expand with temperature and is of utmost importance when constructing a SOC stack. All components must have a matching TEC to avoid mechanical stresses on the stack, as the stack will increase from room temperature to 600-850 ℃. Not matching the TEC of cell components will cause the stack to crack and ultimately break. Early interconnects used ceramic materials and one of the main problems were their TEC. Ferritic stainless steels as an alternative were introduced due to the reduced cost of the material and a more closely matched TEC with the other cell components.[29]

1.2.4 High temperature corrosion

The following section is largely based on the books High-Temperature Oxidation of Metals and Fuel Cell Systems Explained. [22][6]

Corrosion is the natural degradation process that, along with most metals, goes through under standard conditions. The metal is slowly reacting with oxygen to form metal oxides similar to the original ore from which the metal was initially mined. This process is ongoing at ambient temperatures; even though metals such as iron seem stable, they slowly oxidise and form iron oxides such as Fe_3O_4. When metals begin to oxidise, a thin oxide layer is formed on the surface of the metal. This layer slows down the continued corrosion by protecting the metal underneath from further contact with oxygen. Depending on the initial oxide, oxygen will diffuse through the oxide scale and continue to react. At ambient temperatures, this process is slow and can be discounted for many applications, but since SOCs are operating at significantly higher temperatures and in more corrosive environments, corrosion must be taken into account. The increase in the temperature of the system significantly increases the reaction rates and also changes the thermodynamics of the corrosion reacton. To determine the extent of the corrosion, it must be determined whether it is thermodynamically favoured and if so what the kinetics of the reaction are.

1.2.4.1 Thermodynamics/Ellingham diagram

The thermodynamics of the reaction decides whether the reaction is spontaneous under certain conditions, generally described by the concept of Gibbs free energy ΔG. ΔG is the sum of energy in the system described by equation 1.9,

$$\Delta G = \Delta H - T\Delta S \tag{1.9}$$

Where ΔH is the enthalpy, T is the temperature and ΔS is the entropy. Simplified, the enthalpy of a system can be described as its internal energy and can be used to measure changes in energy of the system. The entropy term describes the disorder of the system, where a very structured system such as a crystal has low entropy and a highly unstructured system such as a gas has high entropy. ΔG can also be described in terms of the deviation from the ΔG at standard conditions called ΔG_0,

$$\Delta G = \Delta G_0 + RT * ln(Q) \tag{1.10}$$

Where ΔG_0 is the Gibbs free energy at 25 °Cand 1 atmosphere (atm), R is the gas constant, and Q is the equilibrium constant, further defined in equation 1.11,

$$Q = \frac{a_{products}}{a_{reactants}} \tag{1.11}$$

Q is used here to describe the relation between the chemical activity of products and reactants for a chemical reaction. Looking at a general reaction for the oxidation of a metal, denoted M,

$$x\,\mathrm{M} + \frac{\mathrm{y}}{2}\,\mathrm{O}_2 \rightleftarrows \mathrm{M}_x\mathrm{O}_y \tag{1.12}$$

The reactants M and O_2 react in a specified ratio (x and y) to form a metal oxide M_xO_y. If equation 1.12 is combined with equation 1.11 and then used in the expression for ΔG through equation 1.10, an equation 1.13 describing the Gibbs free energy for the oxide formation reaction is formed,

$$G = G_0 + RTln\frac{a(MxOy)}{a(M)^x * a(O2)^{y/2}} \tag{1.13}$$

This equation can be further developed by using the assumption that a for solids is equal to 1 and that we have reached equilibrium for the reaction, as well as that a for O_2 can be described as partial pressure, $p(O_2)$. The Gibbs free energy can then be correlated with the partial pressure (concentration in the gas phase) of oxygen,

$$pO_2 = \exp\frac{\Delta G * 2}{RT} \tag{1.14}$$

Equation 1.14 can be used to construct an Ellingham diagram. It can be used to visualise how the thermodynamics of the oxide formation reaction changes with temperature and oxygen partial pressure.

The Ellingham diagram has temperature as the x-axis and Gibbs free energy as the y-axis. The Ellingham diagram also has scales for $p(O_2)$, H_2/H_2O, and CO/CO_2 wrapping around it. Equation 1.13 is used to calculate ΔG for the relevant oxides that is plotted in the diagram. Equation 1.14 is incorporated in the diagram through the marked “O” in the upper left corner, from which a line can be drawn to the corresponding pO_2 on the right-hand scale. The intersection formed by this “Oxygen line” and the ΔG line indicates at what temperature the metal will start oxidising. Figure 1.3 visualises the temperature and $p(O_2)$ dependence of some common oxides in an Ellingham diagram.

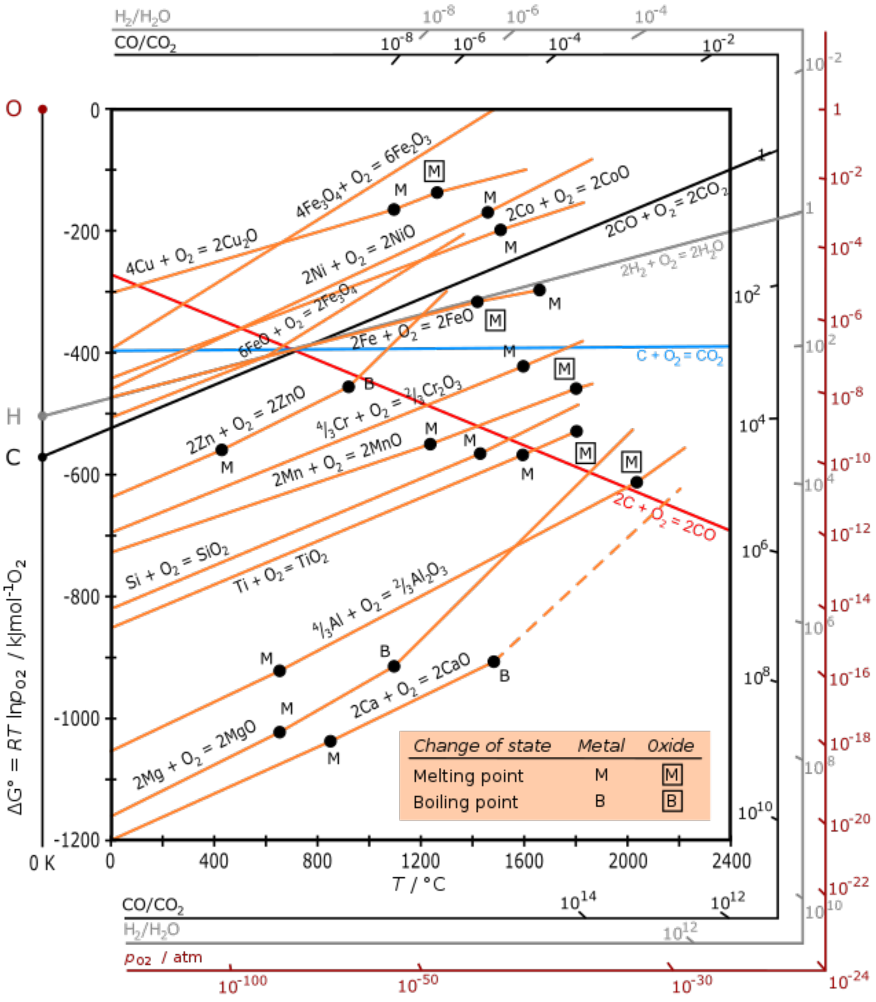

Figure 1.3: Ellingham diagram of common oxides. The x-axis is the temperature in Kelvin, and the y-axis is the Gibbs free energy. When a line is plotted from the oxygen marker (red O in the upper left corner) to the partial pressure scale on the right side of the diagram, the stability of the oxides in the diagram can be determined. Oxide lines below the oxygen line indicate that the oxide is thermodynamically stable while the opposite is true for oxide lines above the oxygen line.

The Ellingham diagram indicates which oxides will form at a certain temperature and partial pressure of oxygen. As an example: at a temperature of 1000K and an oxygen partial pressure of 10^{-22} Bar; MnO and oxides below will be stable, but Cr_2O_3 and oxides above will not be stable and will therefore stay in a metallic state (see appendix figure A.1).

It should be noted that one of the most relevant elements for this work, Fe, has three separate oxides: FeO, Fe_3O_4, and Fe_2O_3. Multiple different versions of iron oxides may form simultaneously if the pO_2 allows. It is also important to note that oxides consisting of multiple metals will also form but are not represented in the Ellingham diagram. Metal oxides of the same crystal structure (spinel structure) such as Mn_3O_4 and Fe_3O_4 will conventionally create a mixed $(Fe, Mn)_3O_4$ oxide.

1.2.4.2 H_2/H_2O environments

For alternative oxidative environments, such as H_2/H_2O and CO/CO_2, the Ellingham diagram introduces alternative lines. Similar to the oxygen line, a line can be drawn from the "H" point in the left part of the diagram to the corresponding H_2/H_2O ratio on the right side. This line represents the oxygen equilibrium reaction (equation 1.15) between water, hydrogen and oxygen.

$$\mathrm{H_2O} \rightleftharpoons \mathrm{H_2} + \frac{1}{2}\mathrm{O_2} \tag{1.15}$$

Which can be expressed in terms of Gibbs free energy as:

$$G = G_0 + RTln(\frac{a(H_2O)}{a(H_2) * a(O_2)^{1/2}}) \tag{1.16}$$

and rearranged (through equation 1.14) into:

$$pO_2 = (\frac{pH_2O}{pH_2})^2 * \exp\frac{-2\Delta G^O}{RT} \tag{1.17}$$

The calculated pO_2 determines which oxides are formed.

1.2.5 Oxides

Metal oxides are formed at the intersection between the metallic material and the atmosphere, creating a barrier that limits the contact of atmospheric gas molecules with the metal surface. As the oxide grows, the reaction rate of further growth is generally decreased. The reaction rate is then mostly determined by diffusion of reactants through the already existing oxide layer. Either the gaseous anions diffuse inwards or the metallic cations diffuse outwards to further the oxide scale formation. The diffusion is mostly determined by defects in the oxide.

1.2.5.1 Defects

All real crystals contain defects to some degree; even oxides that are mainly stoichiometric contain defects, as they are entropically favourable. The amount of defects in a crystal lattice is dependent on temperature, partial pressure of oxygen and the chemical composition of the material. The formation of defects requires energy and therefore an increased number of defects will increase the enthalpy of the system, and according to equation 1.9 there will be an equilibrium between enthalpy and entropy that determines the number of defects.

Defects are one of the main factors contributing to the transport of oxygen and metal ions in the oxide layer. A large number of defects will increase the diffusion rate in the crystal lattice, as there are a larger number of ion and electron holes to move across. The most prominent types are “Schottky” and “Frenkel” defects (visualised in figure 1.4).

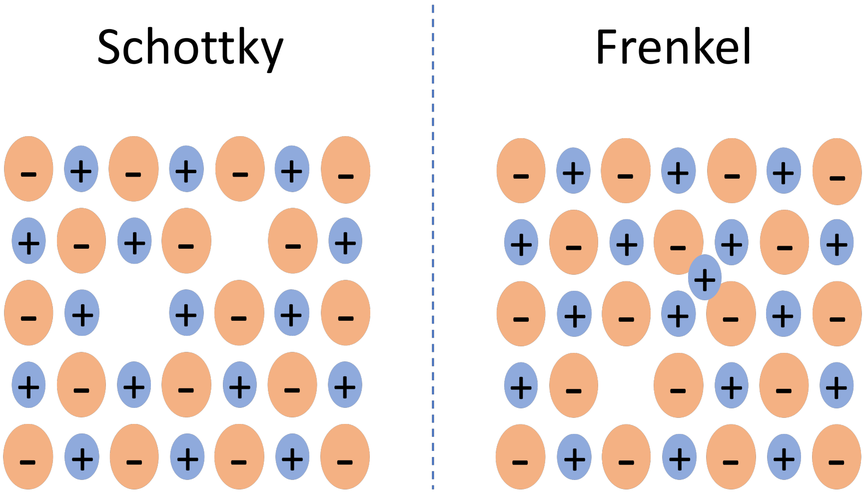

Figure 1.4: Scheme over Schottky and Frenkel defects. Schottky defects are created by the formation of an anion and a cation hole. Frenkel defects are created by a cation moving to an interstitial place in the crystal lattice. Adapted from [22]

.

Both defects consist of ion holes in the crystal lattice formed in such a way that the overall charge is still retained. Schottky defects are created by the formation of an anion and a cation hole while Frenkel defects are created by a cation moving to a interstitial place in the crystal lattice. Both of these defects have the effect of opening up ionic transportation pathways meaning that ions, for example O^{-2}, could move through the crystal by occupying anion holes formed.

1.2.5.2 Chromia

Chromium addition to steel is one of the most well used strategies to decrease corrosion on the material. The reason for this is that Cr oxidises more easily than Fe and forms a thin and dense oxide with the structure Cr_2O_3. This corundum-structured oxide drastically slows down further oxidation, which lengthens the lifetime of the material. The protectiveness of the chromia (Cr_2O_3) is determined by the availability of Cr in the intersection between metal and oxide.

At lower temperatures, diffusion of metals inside the alloy is lower, which creates potential problems of depletion zones as the metal diffuse slower than it oxidises. Depletion zones are created near the surface where e.g. Cr is oxidised at a higher rate than the internal diffusion of Cr to the surface. This leads to lower amounts of Cr in the top layer of the metal.

1.2.5.3 Effects oxidation in H_2/H_2O

Oxidation in H_2/H_2O environments will cause changes in the corrosion behaviour compared to corrosion in air. As discussed in earlier sections, the pO_2 will be substantially lowered and alter the properties of the metal oxides. The source of oxygen will come from H_2O or from oxygen created by the $H_2 - O_2 - H_2O$ equilibrium as there are low amounts of O_2 in the atmosphere. One major effect is the change of diffusion properties in oxides. Hydrogen dissolves into the material and forms interstitial protons and OH groups. These defects tend to increase with lower temperature and higher humidity, changing the characteristics of the material. [23]
Studies on H_2/H_2O environments has shown internal oxidation of Cr increased caused by changed diffusivity and solubility of oxygen in the alloy. There is also an effect of a shifted $H_2 - O_2 - H_2O$ equilibrium at the surface of the material causing an inward flux of oxygen into the alloy.[8] It has also been observed that the effects from H_2/H_2O environments are dependent on temperature. Counter-intuitively corrosion is not worsened with increasing temperature and instead forms a complex system where the dissolution of H_2O and H_2 and the diffusion of oxygen and metal ions compete and interact. [32] [30]

2

Methodology

2.1 Material selection and sample preparation

The materials selected for the study were picked to study certain aspects of the corrosion behaviour in a humid hydrogen environment. Pure Fe samples from HMW Hauner GmbH & Co.KG were used as a reference for a pure Fe-oxide former. Nicrotal alloy (≈80% Ni, ≈20% Cr) was used on the other side of the spectrum, only forming a thin chromia layer and giving insights into how the changing environment affected the corrosion behaviour. The thesis also studied commercial steels with varying chromium compositions. The commercial steels used were Crofer 22 APU and AISI 441. Compositions of the materials used are listed below.

	C	Cr	Fe	S	Mn	Si	Ti	Cu	P	Al	La
Crofer 22 APU (JU)	0.03	20-24	Bal.	0.02	0.3-0.8	0.50	0.03-0.2	0.5	0.05	0.5	0.04-0.2
AISI 441 (AK)	0.03	17.5-18.5	Bal.	0.015	1	1	0.1-0.6	-	0.04	-	-

Table 2.1: Table over the compositions for the commercial steels used in the study.

The metal samples were cut into coupons of 20x10mm with varying thicknesses for the different samples. Samples were placed in an alumina sample holder with slits to contain 9 samples in each sample holder. After the samples were chosen and cut into the correct sizes, they were cleaned by being sonicated in acetone and ethanol for 10 minutes each. The cleaning step was meant to remove dirt or oils on the samples to have a pure metal surface for corrosion exposures.

2.1.1 Pre-oxidation of samples

Pre-oxidation as a means of corrosion protection has been established by a multitude of earlier studies.[28][13] The method was used to increase the corrosion resistance of the alloys as they suffered severe corrosion during the primary experiments. Protective pre-oxidation was carried out in a horizontal tubular furnace at 800 ℃ with a gas flow of 3% H_2O - Air (280 ml / min) for 10, 15, 17, 20, and 30 minutes. The samples were weighed before and after pre-oxidation and then used in exposures.

2.2 Experimental setup

The thesis work was conducted in an experimental setup visualised in figure 2.1 to study the corrosion phenomena in humid environments. The setup used is highly similar to the work of Alnegren et al. [3] as it was used to further study the phenomenon identified at other temperatures.

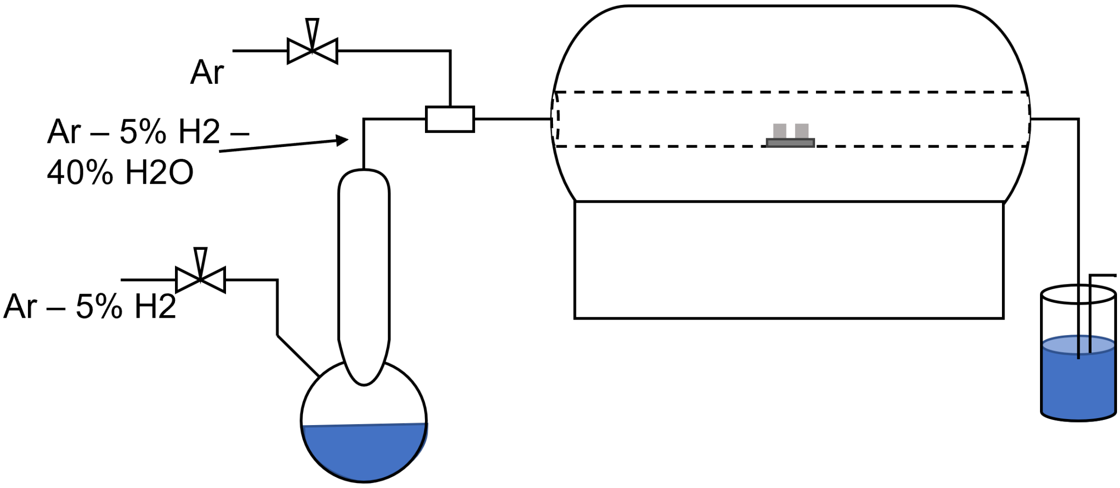

Figure 2.1: Schematic over the experimental setup used during exposures. H_2-Ar gas was humidified, led through a coil condenser and then diluted with Ar-gas before it was led into the furnace.

2.2.1 Initial experiments

The exposures were run in a temperature controlled horisontal tubular furnace. The furnace was fitted with an alumina inner tube into which samples were placed on the alumina sample holders described in Section 2.1. The furnace was fitted with metallic end caps connected to the gas inlet on one end and a bubbler on the other end. The gas inlet consisted of a 5% H_2-Ar line which was led through a humidifier, through a coil condenser, and then mixed in the right proportions with a secondary Ar flow. The humidifier was a round-bottom flask heated to 81 ℃ by a heating mantle and thermally insulated to ensure constant temperature. The coil condenser was connected to the humidifier and had a temperature of 76.3 ℃ which corresponds to 40% water content in the humidified gas flow. The coil condenser was also thermally insulated.

The resulting gas flow had a concentration of 3%H_2, 40% H_2O, and 57% Ar. The gas was then diluted with Ar gas to achieve the correct humidity while the ratio of H_2 to water was kept constant. The gas flow was led through insulated and heated piping into the furnace. The gas outlet from the furnace was bubbled through water to seal the system and to take care of the excess humidity. Figure 2.1 is a schematic of the setup having a gas inlet to the left and the outlet from the furnace on the right. During the thesis work three environments was used: the undiluted 40% water environment, diluted to the 1.5% H_2-20% H_2O-Bal. Ar environment, and diluted to the 0.75% H_2-10% H_2O-Bal. Ar environment. They will from this point forward be called 40%, 20%, and 10% respectively, referring to the water contents. The total flow rate after dilution was kept to 250 ml/min for all environments.

The furnace was purged with 2000 ml/min dry 5%H_2-Ar for a minimum of 30 min before the start of each exposure and after each intermediate weighing of samples during exposures. The furnace was then heated at a rate of 2.5 °C/min. After the intermediate steps of 24h, 72h, and the final 168h the furnace was cooled down by completely turning the heating, resulting in a slower cooling rate than 2.5°C/min.

2.2.2 Gravimetric measurements

The weight measurements gave information on the oxidation of the samples. Before each exposure, samples were cleaned and weighed with a Mettler Toledo XP6. Samples were taken out during the exposures and weighed twice before being put back into the furnace. After the exposures samples were weighed twice to get a final mass gain for the experiment.

2.2.3 SEM/EDX

To further analyse the oxidation of the samples, Scanning Electron Microscope (SEM) was used. SEM is a method of analysing the morphology and composition of the surface of the sample. The working principle of SEM is that an electron beam is directed at a metal sample. The beam interacts with the surface of the sample, mainly by three different mechanisms: secondary electrons, back-scattered electrons, and characteristic X-rays. [26]

Secondary electrons (SE): When the electrons hit a surface they will have inelastic interactions with the electrons of the surface atoms. Simplified, the incoming electrons hits the electron of atoms in the surface resulting in an ejection of electrons from the atom. These electrons are lower in energy than the incoming primary electrons. Edges on the surface will release more secondary electrons compared to flat parts as they can only leave sample near surface and will therefore yield a higher signal. Secondary electrons are used to gain information on the morphology of the sample's surface.

Backscattered electrons (BSE): The incoming primary electrons will also interact elastically with the sample atoms and might get scattered back up from the surface through "back scattering". Larger (heavier) atoms will scatter more electrons back resulting in a stronger signal. BSE can therefore be used to get information the kind of atoms that are present in the sample.

Characteristic X-rays: Another way of detecting different elements in a material is by identifying the characteristic X-rays coming from the material. When the secondary electrons are ejected in the process described above, electrons from higher energy states will fill the vacant spot sending out an X-ray beam in the process. [26] [27]

Together the different signals create an image of the material's surface with information on the surface area of the material.

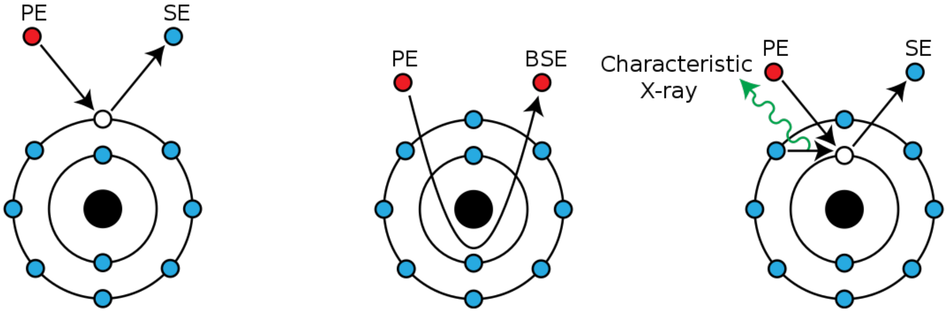

Figure 2.2: The three main mechanisms utilised in SEM: secondary electrons (SE), backscattered electrons (BSE), characteristic X-rays. Reworked from [10]

2.2.4 Cross-section preparation

To create the intersection of the metal oxide layers, broad ion beam (BIB) milling was used. The selected sample was cut with a low speed saw, exposing the cross section. A silicon wafer was placed on top of the oxide surface parallel to the cross-section and glued in place. The cross-section was ground and polished with sandpaper to a fairly smooth surface. The sample was placed onto a sample holder with a silver-based adhesive and then placed inside the BIB milling machine. A vacuum was pulled inside the chamber holding the sample, and the ion milling process was started.

The BIB milling consists of three ion guns that target the sample with an ion beam under high vacuum, removing artefacts that are difficult to remove by mechanical polishing. This process creates an evenness on the nano-scale necessary to get good resolution when using SEM to analyse samples.

2.3 Raman Spectroscopy

Raman spectroscopy was utilised in this work to identify oxides on the exposed samples. The method uses laser light to identify distinct vibrational and rotational modes of the bonds in the oxide crystal structure which works like a structural fingerprint. When the light is shone at the sample surface, the surface oxide will scatter it in a mostly elastical way where light of the same energy will come out as the light going into the material. A small percentage of the incoming photons will however be scattered inelastically where the outgoing light either has a lower or higher energy than the incoming light. This inelastic scattering is called Raman scattering and by analysing the outgoing light from the sample, it is possible to create a graph over the created Raman scattering peaks. As this graph is unique for different molecules, it is possible to identify the sample oxide. [20]

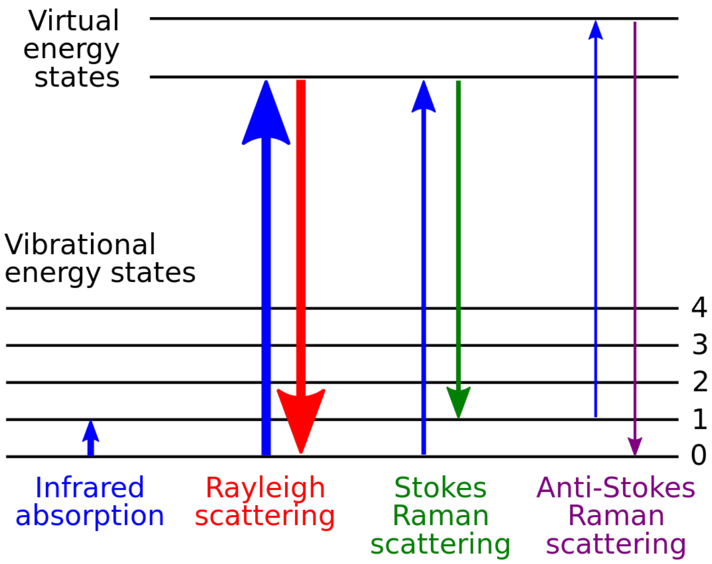

Figure 2.3: The change in energy levels for Raman diffraction. Reworked from [11]

3

Results

3.1 Comparative study of Alnegren et. al

To verify the results of Alnegren as well as to confirm that the experimental setup was reproducible, preliminary experiments were performed. As the perceived effect was most prevalent during the first 24 hours, the reproducing study was performed for 24 hours at 850℃ and the material used was AISI 441. Samples of AISI 441 were exposed at 40% and 10% and the same effect was observed. In Table 3.1 the mass gains are presented.

Temperature	850℃			
Studies	Present study		Alnegren et al.	
Environments	40%	10%	40%	10%
Mass gain average (mg/cm^2)	1,01	0,67	0,4	0,1

Table 3.1: Mass gained at 850 ℃ after 24h for AISI 441 in this thesis project and for Alnegren et al. in in 10% and 40% humidity.

Compared to the Alnegren study, the samples experienced higher oxide growth. Even if the mass gain was substantially higher, a similar difference between the two environments was observed. The shift in mass gain between studies could be attributed to differences in batches of material used or slight differences in setup. As part of a preliminary study, a sample of the AISI 441 was ground to a rough surface and exposed parallel to the “as recieved” samples. The ground samples did show a similar mass gain to what was observed in the Alnegren study suggesting that the surface layer of the “as recieved” samples used in this study might be worse in forming a protective chromia scale than samples used by Alnegren.
As the effect mainly occurs during the first 24 hours, it can be hypothesised that the observed effect originates from the temperature ramping up and/or ramping down. The theory builds upon studies suggesting that corrosion at lower temperatures in H_2/H_2O environments causes worsened corrosion behaviour. This phenomena is not well understood but have attributed to the dissolution of H_2 and H_2O into the material as well as other effects. To test the theory, exposures at 650℃ were executed.

3.2 Exposures at 650 ℃

Alnegren identified the drastic difference in corrosion behaviour between high and low humidity that occurred during the first 24 hours, after which the parabolic oxide growth was similar. This could indicate that the start of the exposure and the subsequent temperature ramping had a larger influence on the mechanism than the temperature set point of 850 ℃.
The samples were therefore exposed at 650 ℃ to explore this hypothesis. The experimental setup was recreated as close as possible to isolate the temperature as a factor. Samples of Crofer 22 APU and AISI 441, as well as Fe and NiCr model alloys, were exposed for 24 h and then weighed.

Both commercial steels experienced severe oxidation and did not show any significant difference between 10%, 20%, and 40%.
To show that no effects to pO_2 are happening when changing the humidity, a pure Fe metal was exposed. As it only forms iron oxides, it should have the same mass gain for all different configurations if pO_2 is constant. The measured mass gain for the iron indicated no correlation to changes in humidity.
The nickel alloy was exposed to show that a protective chromia layer would form in the experimental conditions. The mass gain indicated formation of the expected thin protective chromia layer.
The mass gain data are presented in Table 3.2 below. As both commercial steels experienced break away corrosion, it was determined that the samples needed to be pre-oxidised in a suitable manner to see the prevalence of the dilution effect at 650 ℃.

Environments	10%	20%	40%
Fe (mg/cm^2)	10,14	9,78	9,98
NiCr (mg/cm^2)	0,016	0,038	0,036
Crofer 22 APU (mg/cm^2)	0,84	1,06	1,21
AISI 441 (mg/cm^2)	2,18	2,34	2,21

Table 3.2: Mass gain averages for Fe, NiCr, Crofer 22 APU, AISI 441 in three environments with different humidity's.

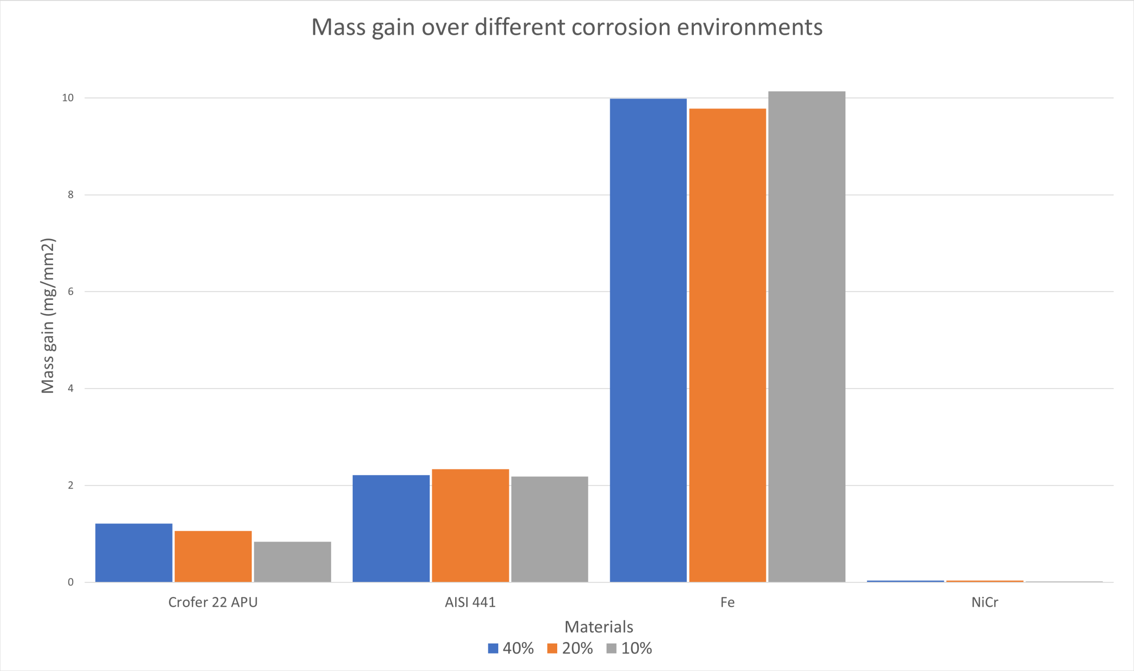

Figure 3.1: 24 h screening test of the two commercial steels AISI 441 and Crofer 22 APU and two model alloys of NiCr and pure Fe in different humidity.

The only material that showed a slight potential correlation of mass gain with humidity was the Crofer 22 APU, but as all samples experienced a high rate of corrosion, it was difficult to draw conclusions from these results. To get clearer results, further experiments were conducted with pre-oxidised samples.

3.3 Pre-oxidised samples

AISI 441 were pre-oxidised and then exposed for 168h in the 10% and 40% environments. Samples were pre-oxidised between 5-20 minutes according to the method described in section 2.1.1. The resulting mass gain taken after 0, 24, 72, and 168 hours is presented in Figure 3.2 below with subfigures 3.2a, 3.2b, and 3.2c representing some of the different pre-oxidation times.

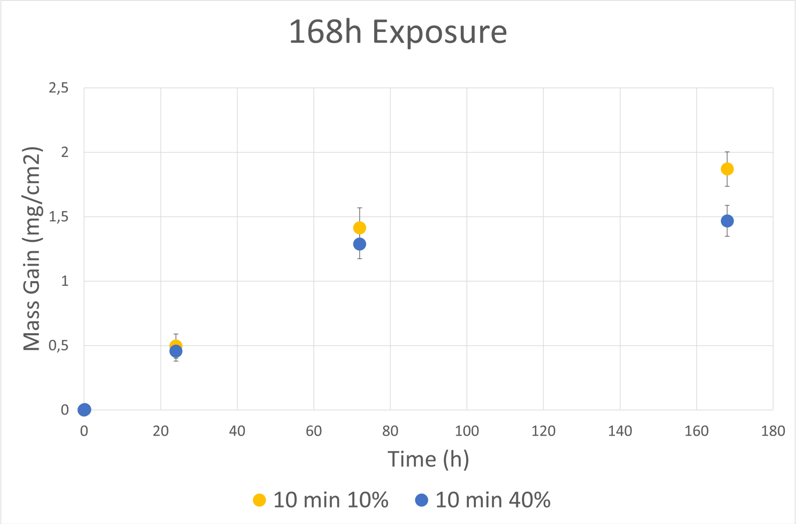

(a) Mass gain over 168 hours for samples pre-oxidised for 10 minutes

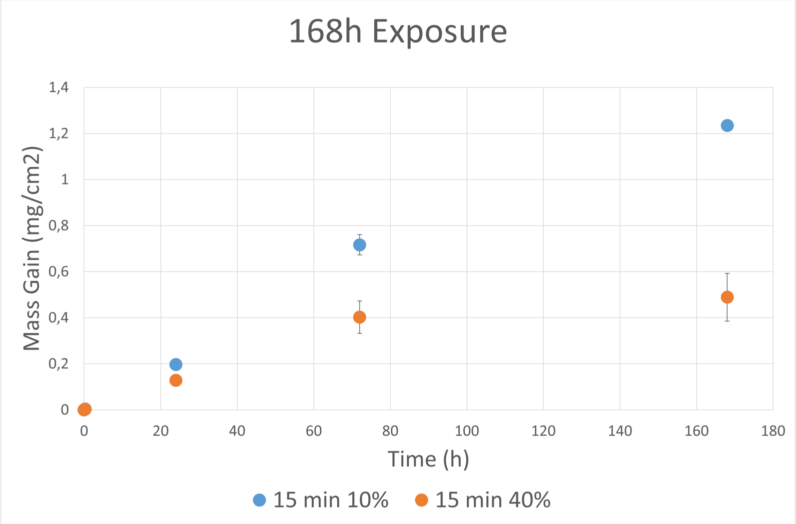

(b) Mass gain over 168 hours for samples pre-oxidised for 15 minutes

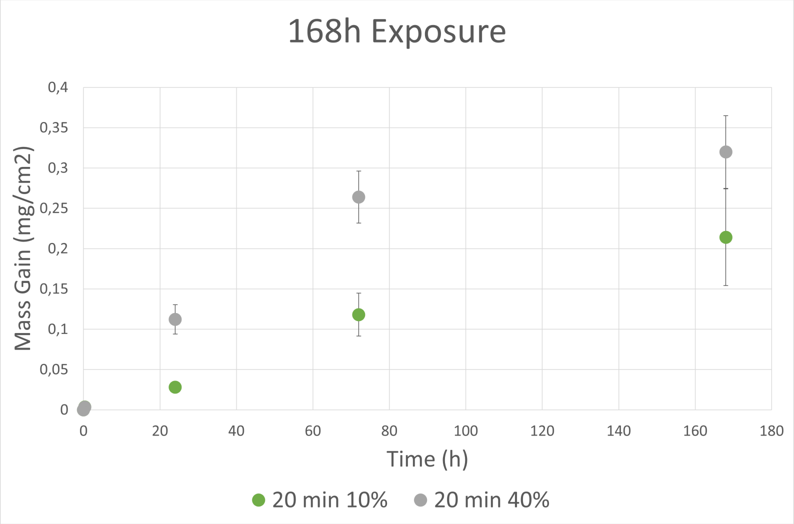

(c) Mass gain over 168 hours for samples pre-oxidised for 20 minutes

Figure 3.2: Exposure over 168h with samples of different pre-oxidation times: a) 10 min, b) 15 min, c) 20 min.

The graphs in Figure 3.2 describe the mass gain over 168h hours for samples with different pre-oxidation times. It can clearly be seen that the protection of the material increase with pre-oxidation time, nevertheless the Δm indicated all samples exhibit breakaway corrosion. The samples with 10 and 15 min pre-oxidation time indicate that the samples exposed to 10% humidity experienced a higher rate of oxidation than those in the 40% environment. The opposite effect is observed for the samples pre-oxidised for 20 minutes. There is also a substantial difference in mass gain between the different 20 minute samples causing slightly overlapping error bars between the 10% and 40% samples. It is important to note that the error bars presented are gathered from a single experimental run with samples sizes of at least 3. Differences between runs might differ more than between samples in the same run and are therefore likely to create larger error bars.

In Figure 3.3, before and after pictures are shown for one of the samples with a 15 minute pre-oxidation time. On the right side of the sample exposed for 168h, a red oxide formed. This oxide was investigated further as it was likely to be Fe_2O_3, an oxide that is not thermodynamically stable in the H_2/H_2O ratio utilised.

(a) A metal coupon of AISI 441 after pre-oxidation in air.

(b) A metal coupon of AISI 441 after a 168h furnace exposure.

Figure 3.3: Before and after image of a metal coupon pre-oxidised and then exposed for 168h in the 10% environment. Before image a) shows a thin protective oxide layer which will slow down further oxidation. b) Shows the coupon after 168h. Red oxide has formed on the right most and top edge of the sample, where the gas flow first comes in contact with the metal.

The red oxide was mainly seen on the samples which were closest to the gas inlet, and it formed mainly on the edges which first came in contact with the gas flow (as seen in Figure 3.3b). This uneven oxide formation might be caused by some secondary effect connected to gas transport over the sample holder.

3.3.1 Oxide Identification

There are three different iron oxides, Fe_2O_3 (hematite), Fe_3O_4 (magnetite), and FeO (wüstite) which are know to form from high temperature corrosion. Visual inspection suggested that the red oxide was Fe_2O_3, as literature indicated it would be the only one that could form red oxides. To identify the red oxide, SEM and Raman spectroscopy were used.

3.3.1.1 SEM

SEM was used to identify the different oxide layers and their thickness. Figure 3.4 show a SEM image of red oxide.

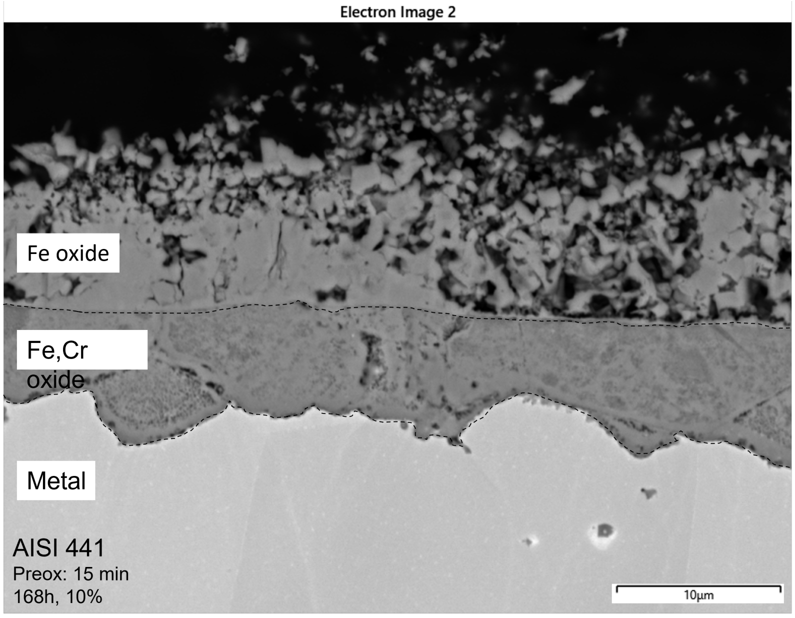

Figure 3.4: A SEM image of the cross-section of the oxide scale in the red part of the sample from Figure 3.3b

The SEM image identified two discrete oxide layers: one outward growing, mainly consisting of Fe, and one inward growing, consisting of a combination of Cr and Fe. A SEM image of the black oxide scale was also taken to identify potential differences, presented in Figure 3.5.

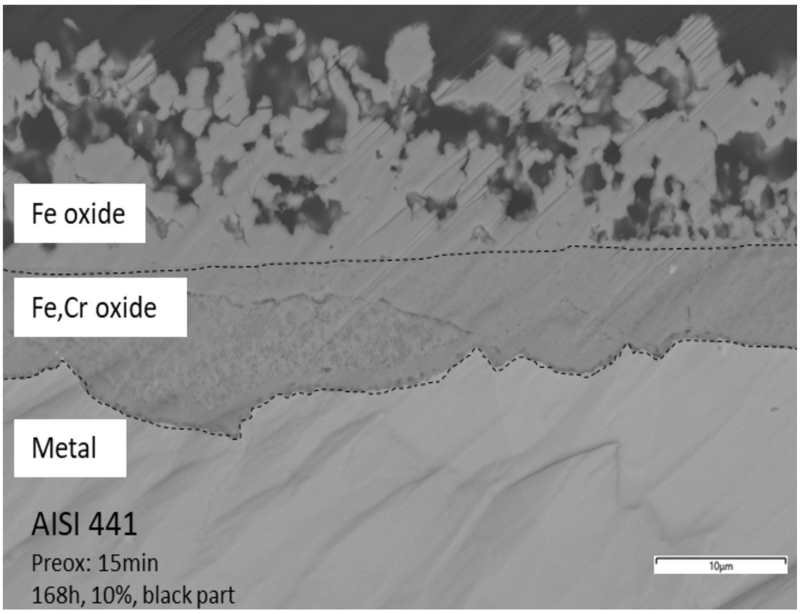

Figure 3.5: A SEM image of the cross-section of the oxide scale in the black part of the sample from figure 3.3b

The SEM images of the black and red parts are similar with the same composition and oxide scale thickness. The differences between the images can be seen in the Fe oxide, the porosity of the oxide is different between the sites. The red site Fe oxide is a lot more porous which was also seen during initial inspection where red oxide easily fell of the sample. The black site oxide were more coherent and less porous. According to literature, Fe_2O_3 can have a black colour in mineral form but will form a red oxide when ground to a powder.[7][25] The difference in porosity between the samples might be the reason behind the colour difference shown in figure 3.3b.
During the SEM analysis, Energy Dispersive X-ray Spectroscopy (EDX) was used to get information on the chemical composition of the oxide layers. With EDX, the approximate atomic composition of the oxide layers were identified. The theoretical atomic compositions of some expected oxides are described in Table 3.3.

Oxides	Fe	Cr	O
Fe_2O_3	40%	-	60%
Fe_3O_4	43%	-	57%
Cr_2O_3	-	40%	60%
$(Cr, Fe)_3O_4$	0-43%	0-43%	57%

Table 3.3: Theoretical atomic composition of relevant oxides.

The EDX indicated that the Fe/Cr oxide is $(Fe, Cr)_3O_4$ and that the Fe oxide layer could be Fe_2O_3 for both red and black sites but did not have a perfect correlation. In Figures 3.6a, 3.6b, and 3.6c EDX graphs are shown with the different oxide phases for the red site. Further EDX information is found in appendix A.3.

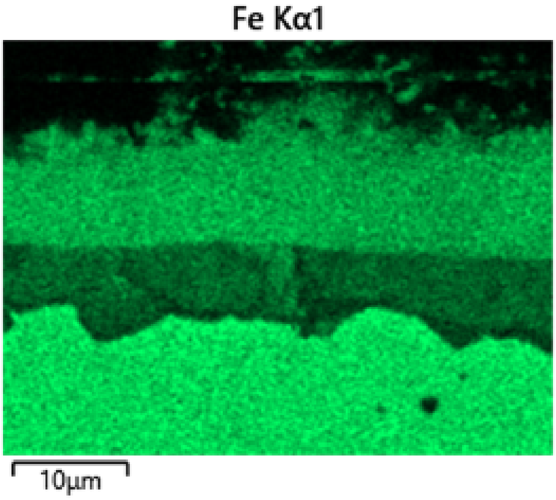

(a) Fe in the red oxide sample.

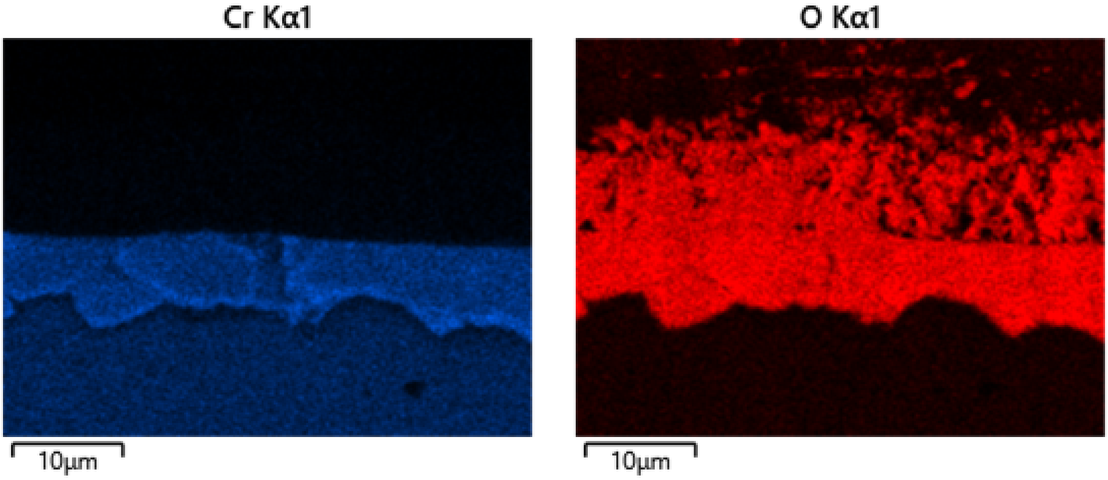

(b) Cr in the red oxide sample.

(c) O in the red oxide sample.

Figure 3.6: EDX of the red oxide on the sample shown in figure 3.3b with a) Fe, b) Cr and c) O.

The chemical composition of Fe_2O_3 and Fe_3O_4 is fairly similar and therefore it was necessary to complement the analysis with Raman spectroscopy.

3.3.1.2 Raman Spectroscopy

Raman spectroscopy was performed on multiple points of the sample shown in Figure 3.3b, on both red and black parts of the material.

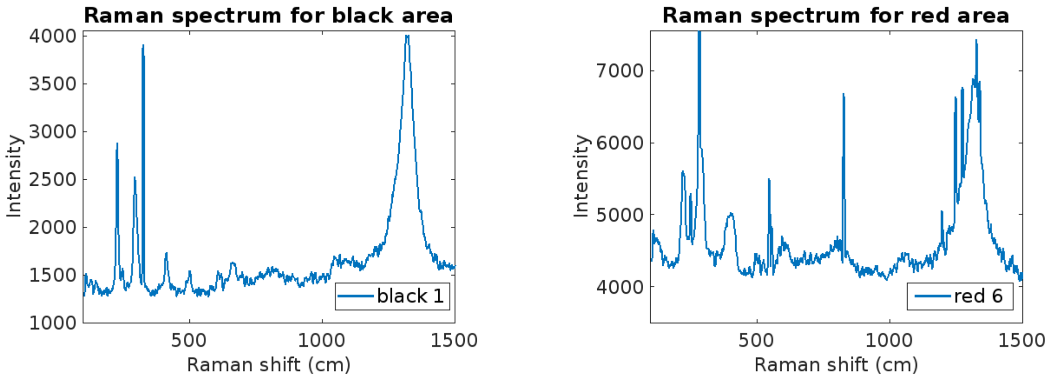

(a) **(b)**

Figure 3.7: Raman spectrum of the a) black oxide and b) red oxide

The analysis revealed that both areas were covered by Fe_2O_3, as the spectra share the same peaks corresponding to the oxide. A table over the peaks associated with Fe_2O_3 are presented in Table A.1 in Appendix A1.

3.3.2 Making sense of the hematite formation

Connecting the oxide back to thermodynamics and the Ellingham diagram, it is clear that for the specific H_2/H_2O ratio utilised, Fe_2O_3 is not thermodynamically stable. The H_2/H_2O ratio used in the experiment corresponds to a pO_2 of 10^{-20} bar at 650°C , and to form Fe_2O_3 a pO_2 of 10^{-14} is needed. Some effect is creating a raised pO_2 in the furnace causing the samples to oxidise into Fe_2O_3 over the length of the experiment.
The formation of Fe_2O_3 indicates that something is changing the p(O_2) from the initial atmosphere applied. It is unknown what causes this effect, although multiple theories might explain the behaviour. One possible cause is that the temperature of 650 °C is affecting the water equilibrium reaction (described in equation 1.15) so that the gas is not reaching chemical equilibrium before reaching the samples. The gas sources used might have small amounts of oxygen contamination which could worsen this effect. The argon bottles used are standardised to be 99,98% pure meaning that there might be some contaminants present. There is also a possibility of leaks or other defective equipment causing a raised pO_2. To minimise the risk of such effects, the temperature and humidity was measured and the setup was leak tested. Hydrogen might also affect the reaction dynamics in some manor causing local variations of pO_2 making hematite formation possible. It would have been useful to also measure the pO_2 but due to the specific environments and setup used, there was a risk of damaging the O_2 sensor.

3.4 Platinum catalysed exposure

To investigate the potential lack of equilibrium in the gas-mix, a piece of Pt was added with the purpose of catalysing the reaction. Pt is an excellent catalyst for a wide variety of reactions and was added in this context to speed up the reaction rate for the equilibrium reaction. Another 168h exposure of AISI 441 in the 10% and 40% environments at 650 ℃ was executed. In Figure 3.8c, the mass gain for three different pre-oxidation times (17, 20, and 30 minutes) are presented. The changed pre-oxidation times were used to try to increase the protection effect of the samples.

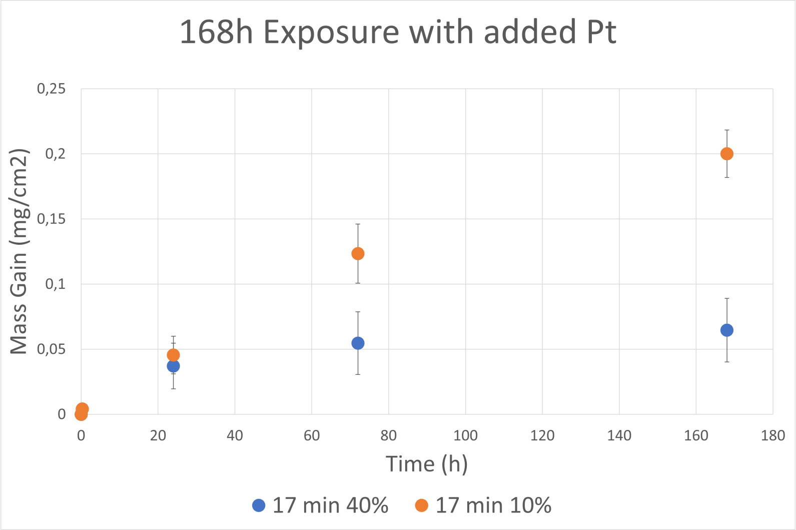

(a) Mass gain plot for samples pre-oxidised for 17 minutes during a 168 hour exposure with a added Pt catalyst.

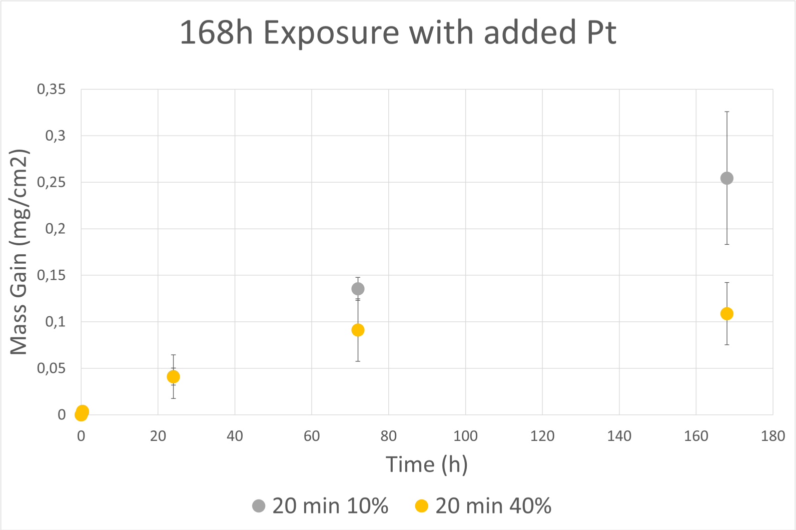

(b) Mass gain plot for samples pre-oxidised for 20 minutes during a 168 hour exposure with a added Pt catalyst.

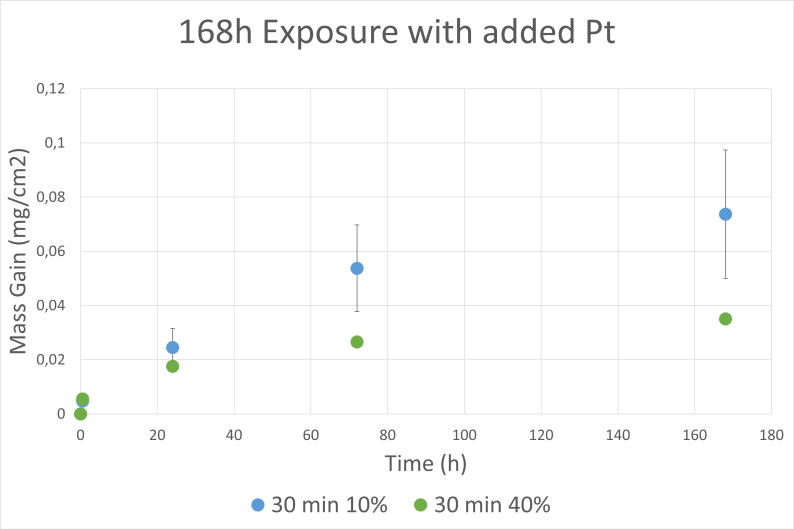

(c) Mass gain plot for samples pre-oxidised for 30 minutes during a 168 hour exposure with a added Pt catalyst.

Figure 3.8: Exposure with added Pt over 168h with samples of different pre-oxidation times: a) 17 min, b) 20 min, c) 30 min.

It was observed that the general mass gain is lowered for most of the samples compared to the conventional pre-ox exposure. Comparing the 20 minute pre-oxidation for a conventional and a platinum catalysed run, the 40% environment caused the mass gain of 0,214 and 0,109 mg/cm^2 respectively. For the 10% environment the mass gains were 0,214 and 0,254 mg/cm^2 respectively. A large decrease was seen in the 40% environment and the 10 % environment saw a slight increase but was still inside of the error margin.

As observed from the graph, the 10% humidity caused a higher mass gain than that of the 40%. This is contrary to the previous results presented by Alnegren et al. and opposes the suggested effect of higher humidity causing a higher rate of oxidation. This reversed effect was observed for all pre-oxidised samples except for the 20 minute pre-oxidation time when running without Pt.

Although the overall oxide growth is decreased compared to the Pt-free exposure, visual inspection indicated that red oxide is still present, meaning that Fe_2O_3 still formed. It is unclear if the Pt actively reduced $p(O_2)$, in accordance with the above-mentioned theory, and further experiments are required to understand the underlying reason behind the formation of the hematite.

4

Discussion

4.1 Formation of Fe_2O_3

The unexpected formation of Fe_2O_3 changed the focus of the thesis work. It is difficult to get reliable data regarding the dilution effect when the additional effect of hematite formation was observed. The focus shifted from deeper investigation of the previously studied dilution effect to further studying and potential mitigation of the Fe_2O_3 formation. The most likely candidate was decided to be a non equilibrium gas mixture due to the lower temperature. Through the addition of Pt into the furnace, the theory of the shifted equilibrium in the gas mix was tested. The Pt was supposed to catalyse the gas mix equilibrium reaction. The addition of Pt did change the mass gain compared to a conventional exposure but did not completely stop the formation of hematite. As the added Pt was in a solid piece and not optimised to be a catalyst, the underlying reason behind why it did not work to hinder hematite formation could be that of not working efficiently enough. It would be of interest to measure the O_2 concentration in the furnace inlet, hot zone, and outlet with and without Pt to see eventual effects. This would be experimentally difficult but could provide an adequate answer to the question of hematite formation.

There are other potential effects which were not explored in this thesis work e.g. hydrogen effects in the material. There are substantial evidence that hydrogen alters the corrosion behaviour, worsening corrosion in exposures where a sample is exposed to both a fuel atmosphere and an oxygen atmosphere (dual atmosphere). This dual atmosphere effect was observed to be more active at 650 ℃ than higher temperatures. This effect has not been proven to change pO_2 but might play a role in the overall effect.

4.2 Comparative study

The comparative study was able to qualitatively replicate the results of Alnegren et al. although observed mass gain data differed substantially. It is difficult to discern the reason behind this discrepancy as there could be multiple underlying reasons. Material differences are likely to play a role in the differing corrosion behaviour. The material, production batch, and pre-treatment will affect the behaviour in a corrosion exposure and differences was tried to be reduced. As mentioned in 3.1 the sample ground to a rougher surface did get the same mass gain as samples in the Alnegren study.

There is also the possibility that the experimental setup varied in some minor ways.

The setup was replicated to the extent possible from the description in the research article such as heating, cooling, and flow rates. Even so, it is not guaranteed that all aspects match completely.

4.3 Dilution Effect

The thesis work was not able to confirm that an increase in humidity is affecting the corrosion behaviour for low Cr steels at 650°C. In fact, the opposite effect was observed where all samples except one grouping underwent a higher rate of oxidation at lower humidity (10%) compared to higher humidity (40%). It is likely that the formation of hematite (implied raise in pO_2) play a role in these results and they are therefore not completely comparable to the results of Alnegren.

All 168h exposures were done on pre-oxidated samples as the unprotected ones had a rate of oxidation too high for long-term exposures. Some of the exposures were done with the addition of Pt into the furnace. This Pt addition should not affect the corrosion behaviour, except in the ways explained above, but this can not be completely excluded. When looking at these 168h exposures, all but the 20 min pre-oxidation samples in the conventional exposure indicated that diluting the H_2/H_2O environment from 40% to 10% with Ar caused a higher rate of oxidation.

This raises questions about standardisation of experimental protocols. The studied systems suffer from high complexity making it difficult to recreate experiments and to isolate distinct factors. The use of diluted fuel environments is practical from a safety standpoint but the reliability of the results from these kind of experiments must be verified and compared to applied conditions in real electrolysers. In industry conditions, pure steam with some addition of hydrogen is applied on the fuel side. This environment requires safety precautions which make it difficult to study in a research setting. Diluting it have the potential of enabling research into the area to a greater extent but as the dilution seems to have a tangible effect on the corrosion behaviour, this needs to be reevaluated.

4.4 Future work

It is of high importance to study corrosion phenomena in electrolysis environments as it is needed to make the technology commercially viable. The need for green hydrogen described in the introduction calls for mature technologies that can efficiently produce large amounts of hydrogen. Interconnect materials for SOFC applications are far more studied even if the field still requires further research. The interest in green hydrogen requires the development of SOECs and therefore research into how metallic materials handle electrolysis environments. This thesis opens up for a multitude of different paths to explore further in the endeavour to understand and reduce corrosion in electrolysers.

The dilution effect described by Alnegren still needs to be further studied, starting at the temperature 850°C and investigating other parameters. Removing or reducing the heat ramping might determine what effect the lowered temperature does have. It should also be of interest to study the potential difference between lab exposures and applied conditions as discussed above, to confirm the validity of the dilution method at large.

It would also be of interest to investigate the underlying reasons behind the formation of hematite, if it is an effect of the applied environment or if it is an effect caused by the experimental setup at the specific temperature. As discussed above, it would be useful to be able to measure the pO_2 at various points in the furnace to get a deeper understanding of the hematite formation.

5

Conclusion

The thesis work was done to increase the understanding around corrosion behaviour in Solid Oxide Electrolysis (SOE) environments, with a focus on the fuel side environment (H_2/H_2O). The experimental work studied the effect of the total pressure of H_2/H_2O and the dilution of the gas mix on the corrosion behaviour. Earlier experiments had indicated that increased humidity (increased total pressure of H_2/H_2O) worsened the corrosion behaviour for some of the materials tested. This thesis work has further investigated how the dilution of simulated electrolysis fuel environments (H_2/H_2O) with argon affects ferritic stainless steels. The effects were studied at lower temperature than tested in earlier studies. The experimental study found that severe corrosion at the temperature of 650 ℃ compared to the comparable exposure at 850℃. The lowered temperature caused all samples to form iron rich, fast growing and non-protective oxide scales compared to the protective oxides generally formed at 850 ℃. Further studying of the materials required pre-oxidation as a protective measure due to the harsh corrosion environment.

The 168h exposures resulted in the formation of hematite on some of the samples which should not have been thermodynamically stable in the active corrosion environment. To study and possibly reduce the hematite formation, platinum was added to the furnace as a catalyst to reactions in the gas mix before reaching the samples. The results from the Pt-exposures indicated that the corrosion had lessened but hematite was still present in the samples.

The overall mass gain for the 168h exposures indicated that lower humidity environments performed worse than high humidity environments at the specific temperature range. Due to the hematite formation, it is difficult to further compare the corrosion behaviours between temperatures. The thesis work show the importance of studying corrosion phenomena in these environments as many effects are still not well understood, hindering further development of fuel cell and electrolysis technology.

Bibliography

[1] Iea - International Energy Agency. *Global EV Outlook 2023: Catching up with climate ambitions.* Tech. rep. 2023. URL: `www.iea.org`.

[2] Iea - International Energy Agency. "Global Hydrogen Review 2022". In: (2022). URL: `www.iea.org/t&c/`.

[3] Patrik Alnegren and Chalmers tekniska högskola. *Corrosion of Ferritic Stainless Steel Interconnects for Solid Oxide Cells : Challenging Operating Conditions.* ISBN: 9789175977485.

[4] Arnab Choudhury, H. Chandra, and A. Arora. "Application of solid oxide fuel cell technology for power generation—A review". In: *Renewable and Sustainable Energy Reviews* 20 (Apr. 2013), pp. 430–442. ISSN: 1364-0321. DOI: `10.1016/J.RSER.2012.11.031`.

[5] G. Collodi. "Hydrogen production via steam reforming with CO<inf>2</inf> capture". In: *Chemical Engineering Transactions* 19 (2010), pp. 37–42. DOI: `10.3303/CET1019007`.

[6] Andrew L. Dicks and David A. J. Rand. *Fuel Cell Systems Explained.* 3rd. Wiley, Apr. 2018. ISBN: 9781118613528. DOI: `10.1002/9781118706992`.

[7] M D Dyar et al. *Mineral Spectroscopy: A Tribute to Roger G. Bums Why hematite is red: Correlation of optical absorption intensities and magnetic moments of Fe 3 + minerals.* Tech. rep.

[8] E. Essuman et al. "The effect of water vapor on selective oxidation of Fe-Cr alloys". In: *Oxidation of Metals* 69.3-4 (Jan. 2008), pp. 143–162. ISSN: 0030770X. DOI: `10.1007/S11085-007-9090-X/FIGURES/14`. URL: `https://link.springer.com/article/10.1007/s11085-007-9090-x`.

[9] D. L. A. de Faria, S. Venâncio Silva, and M. T. de Oliveira. "Raman microspectroscopy of some iron oxides and oxyhydroxides". In: *Journal of Raman Spectroscopy* 28.11 (Nov. 1997), pp. 873–878. ISSN: 0377-0486. DOI: `10.1002/(SICI)1097-4555(199711)28:11<873::AID-JRS177>3.0.CO;2-B`.

[10] *File:Electron emission mechanisms.svg - Wikimedia Commons.* URL: `https://commons.wikimedia.org/wiki/File:Electron_emission_mechanisms.svg`.

[11] *File:Raman energy levels.svg - Wikimedia Commons.* URL: `https://commons.wikimedia.org/wiki/File:Raman_energy_levels.svg`.

[12] Dolf Gielen et al. "Renewables-based decarbonization and relocation of iron and steel making: A case study". In: *Journal of Industrial Ecology* 24.5 (Oct. 2020), pp. 1113–1125. ISSN: 15309290. DOI: `10.1111/JIEC.12997`.

[13] Claudia Goebel et al. "The effect of pre-oxidation parameters on the corrosion behavior of AISI 441 in dual atmosphere". In: *International Journal of*

Hydrogen Energy 43.31 (Aug. 2018), pp. 14665–14674. ISSN: 0360-3199. DOI: 10.1016/J.IJHYDENE.2018.05.165.

[14] *Growth in primary chemical production in the Net Zero Scenario, 2000-2030 – Charts – Data & Statistics - IEA*. URL: https://www.iea.org/data-and-statistics/charts/growth-in-primary-chemical-production-in-the-net-zero-scenario-2000-2030-2.

[15] E. Hazan, Y. Sadia, and Y. Gelbstein. "Characterization of AISI 4340 corrosion products using Raman spectroscopy". In: *Corrosion Science* 74 (Sept. 2013), pp. 414–418. ISSN: 0010-938X. DOI: 10.1016/J.CORSCI.2013.05.002.

[16] J D Holladay et al. "An overview of hydrogen production technologies". In: (). DOI: 10.1016/j.cattod.2008.08.039.

[17] *Hydrogen - IEA*. URL: https://www.iea.org/energy-system/low-emission-fuels/hydrogen.

[18] *Hydrogen Generation Market Size, Share & Trends Analysis Report By System (Merchant, Captive), By Technology (Steam Methane Reforming, Coal Gasification), By Application, By Source, By Region, And Segment Forecasts, 2023 - 2030*. Tech. rep. Grand View Research, 2021. URL: https://www.grandviewresearch.com/industry-analysis/hydrogen-generation-market#.

[19] *Hydrogen Production: Natural Gas Reforming | Department of Energy*. URL: https://www.energy.gov/eere/fuelcells/hydrogen-production-natural-gas-reforming.

[20] Daniel J. Johnson, Darren L. Oatley-Radcliffe, and Nidal Hilal. "State of the art review on membrane surface characterisation: Visualisation, verification and quantification of membrane properties". In: *Desalination* 434 (May 2018), pp. 12–36. ISSN: 00119164. DOI: 10.1016/j.desal.2017.03.023.

[21] Joel Martinez-Frias, Ai Quoc Pham, and Salvador M. Aceves. "A natural gas-assisted steam electrolyzer for high-efficiency production of hydrogen". In: *International Journal of Hydrogen Energy* 28.5 (May 2003), pp. 483–490. ISSN: 0360-3199. DOI: 10.1016/S0360-3199(02)00135-0.

[22] Neil Birks, Gerald H. Meier, and Frederick S. Pettit. *High-Temperature Oxidation of Metals*. 2nd. Cambridge University Press, 2009.

[23] W. J. Quadakkers and J. Zurek. "Oxidation in Steam and Steam/Hydrogen Environments". In: *Shreir's Corrosion* (Jan. 2010), pp. 407–456. DOI: 10.1016/B978-044452787-5.00022-6.

[24] Hannah Ritchie, Max Roser, and Pablo Rosado. "CO2 and Greenhouse Gas Emissions". In: *Our World in Data* (May 2020). URL: https://ourworldindata.org/co2-and-greenhouse-gas-emissions%20https://ourworldindata.org/emissions-by-sector.

[25] *Rock Science: The Colors of Hematite | Rock & Gem Magazine*. URL: https://www.rockngem.com/rock-science-the-colors-of-hematite/.

[26] *Scanning Electron Microscopes (SEM) | Science Basics | Products | JEOL Ltd.* URL: https://www.jeol.com/products/science/sem.php.

[27] *Scanning Electron Microscopes | Thermo Fisher Scientific - SE*. URL: https://www.thermofisher.com/se/en/home/electron-microscopy/products/scanning-electron-microscopes.html.

[28] Belma Talic et al. “Effect of pre-oxidation on the oxidation resistance of Crofer 22 APU”. In: *Corrosion Science* 138 (July 2018), pp. 189–199. ISSN: 0010-938X. DOI: `10.1016/J.CORSCI.2018.04.016`.

[29] F Tietz. “Thermal Expansion of SOFC Materials”. In: *Ionics* 5 (1999).

[30] Bent Tveten, Gunnar Hultquist, and Truls Norby. *Hydrogen in Chromium: In¯ uence on the High-Temperature Oxidation Kinetics in O2 , Oxide-Growth Mechanisms, and Scale Adherence.* Tech. rep., p. 1999.

[31] “World Energy Outlook 2022”. In: (). URL: `www.iea.org/t&c/`.

[32] D. J. Young et al. “Temperature dependence of oxide scale formation on high-Cr ferritic steels in Ar–H2–H2O”. In: *Corrosion Science* 53.6 (June 2011), pp. 2131–2141. ISSN: 0010-938X. DOI: `10.1016/J.CORSCI.2011.02.031`.

A

Appendix 1

A.1 Thermodynamics/Ellingham diagram

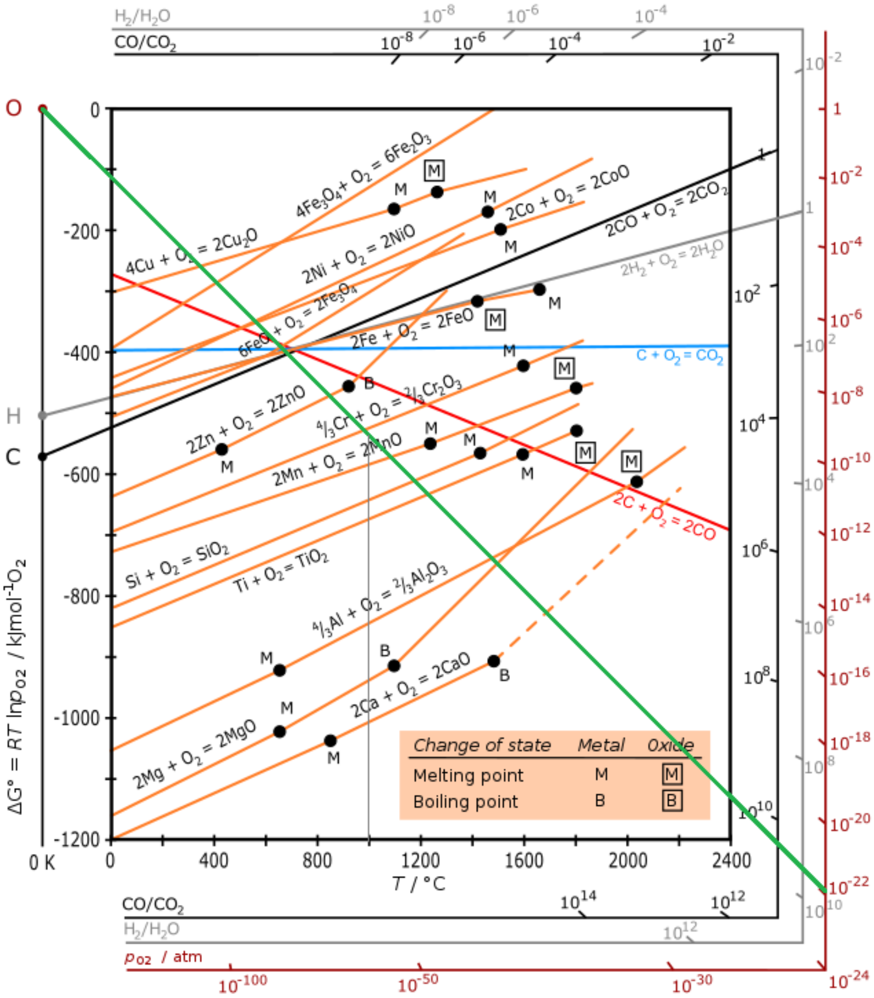

Figure A.1: Ellingham diagram example for the pO_2 of 10^{-22}.

A.2 Raman spectroscopy

	Raman shift (cm)								
Fe_2O_3	226	245	292	299	410	490	610	970	1350
Fe_30_4	300	320	420	470	550	676			

Table A.1: Theoretical Raman shift peaks for hematite (Fe_2O_3) [9] [15]

A.3 EDX values for the Red oxide site.

Spectrum Label	**O**	**Cr**	**Fe**	**Total**
Map Sum Spectrum	47,89	9,82	42,3	100
Red oxide	64,35	0,62	35,02	100
Unknown phase	65,14	22,2	12,67	100
Fe/Cr Spinel	66,2	15,84	17,96	100
Red oxide	65,7	0,32	33,98	100
Unknown phase	64,24	24,08	11,69	100

DEPARTMENT OF SOME SUBJECT OR TECHNOLOGY
CHALMERS UNIVERSITY OF TECHNOLOGY
Gothenburg, Sweden
www.chalmers.se

CHALMERS
UNIVERSITY OF TECHNOLOGY